Kinetic saturation of the Weibel instability in a collisionless plasma

F. Califano,[1] F. Pegoraro,[2] S. V. Bulanov,[3] and A. Mangeney[4]
[1]*Department of Astronomy, University of Florence and INFM, Pisa, Italy*
[2]*Department of Physics, University of Pisa and INFM, Pisa, Italy*
[3]*General Physics Institute, RAS, Moscow, Russia*
[4]*Observatoire de Paris (DESPA), Meudon, France*
(Received 6 November 1997)

We investigate the nonlinear saturation of the Weibel instability in an initially unmagnetized plasma in which two electron streams propagate in opposite directions. We then estimate the fraction of the kinetic energy of the counter-streaming electrons that is transformed by the instability into magnetic energy. In a fluid cold plasma description this instability evolves nonlinearly into smaller and smaller spatial scales. The introduction of a kinetic plasma description resolves these spatial singularities and shows that the instability saturates when the effective electron gyroradius in the generated magnetic field becomes of the order of the electron collisionless skin depth. This corresponds to an approximate energy equipartition.
[S1063-651X(98)00706-5]

PACS number(s): 52.35.Qz, 52.35.Mw, 52.40.Nk, 52.65.Kj

I. INTRODUCTION

The process of magnetic field generation in a plasma and its related inverse process, magnetic field annihilation due to field line reconnection in the presence of current gradients, represent two of the most important problems for both laboratory and astrophysical plasmas. In the lower frequency range, magnetic fields emerge as the dominant factor in the plasma dynamics as a consequence of the effective cancellation of the electric forces due to plasma quasineutrality. At higher frequencies, where this cancellation does not occur, the role of magnetic fields is enhanced in the presence of fast particles. This is particularly true for ''relativistic'' plasmas where the magnetic part of the Lorentz force on the electrons becomes comparable to the electric part. These conditions are realized, for example, in laboratory plasmas interacting with subpicosecond, multiterawatt laser pulses up to 10^{19-21} W/cm^2 [1].

In ''relativistic'' laser pulse regimes, quasistatic magnetic fields can achieve very large intensities as high as 10^5 T with important effects on the plasma dynamics, energy transport and on the propagation and focalization of the laser pulse itself. These quasistatic magnetic fields may have important implications in inertial fusion experiments by focusing and channeling the electromagnetic energy deep inside the pellet in an overdense plasma, as required, for example, in the fast ignitor scheme [2]. In an underdense plasma such magnetic fields may also be responsible for the radial focusing of a fast particle beam in a laser particle accelerator [3–5]. Several mechanisms of magnetic field generation have been analyzed (see Ref. [6] and references therein) that are effective in different plasma regimes. At high frequencies, i.e., on short time scales over which the ions can be assumed to be immobile and collisions are unimportant, the Weibel instability [7] can efficiently generate magnetic fields in plasmas with an anisotropic electron momentum distribution [8].

Recently the role of this electromagnetic-type instability has been reexamined [9,10], in connection with the creation of a magnetic wake behind an ultrashort laser pulse with relativistic amplitudes propagating in an underdense plasma. It was proposed [9] that under such conditions, behind the ultrashort laser pulse, the breaking of the Langmuir wave generates a stream of very fast electrons. Due to plasma quasineutrality, an opposite electron stream must be produced in order to maintain a null total net current (the ions are assumed to be at rest). The quasistatic magnetic field trailing behind the pulse was then interpreted as the result of the repulsion between the current of the fast electrons and the oppositely directed return current carried by the background electrons. In this model, the anisotropy associated with the electron streams represents the external source of free (kinetic) energy able to feed magnetic fields. This is the physical mechanism that drives the Weibel instability: when the electric currents carried by the electron streams are displaced, one with respect to the other, by a transversal disturbance the repulsion of the two oppositely directed currents reinforces the initial displacement. As a result the magnetic field grows in time.

The dynamics of the Weibel instability in an inhomogeneous collisionless plasma was analyzed in Ref. [11] in the framework of a fluid-type description involving two electron fluids, describing the initially counter-streaming electron beams, plus a neutralizing background of immobile ions. It was shown that the development of the Weibel instability is strongly nonuniform and that a spatial resonant-type singularity is formed. The largest magnetic field is generated around this singularity. A first analysis of the nonlinear behavior of the Weibel instability in an initially homogeneous dissipationless plasma was presented in Ref. [12] within the same fluid framework. In this case increasingly small spatial scales were shown to be formed as a consequence of the nonlinear development of the instability.

In the present paper, we discuss the nonlinear evolution of the Weibel instability for perturbations of initial wavelengths much larger or comparable to the electron collisionless skin depth d_e. This length plays the role of the natural scale length for the instability and will be used in the following as the normalization length.

Using a fluid approximation for each of the two electron populations, we investigate the nonlinear evolution of the

Weibel instability that leads to the formation of singularities in a finite time.

In order to study the role of kinetic effects on the evolution of the Weibel instability and, in particular, on the formation of the singularities, we have integrated numerically the Vlasov equation coupled to the Maxwell equations.

First, in Sec. II, we briefly recall the two-fluid electron equations (see also Ref. [11]), and the linear dispersion equation valid for infinitesimal perturbations in the nonrelativistic limit. Then we study the nonlinear evolution of these perturbations both analytically (in the limit of strongly asymmetric beams) and numerically, using initial value simulations. The analytical solutions are used to identify the basic trends in the nonlinear evolution of the instability that are seen in the numerical simulations. In Sec. III we introduce the kinetic Vlasov-Maxwell system of equations and solve them numerically varying the wavelength of the initial perturbation and the mean velocity of the initial electron streams. In Sec. IV conclusions are drawn about the efficiency of the magnetic field generation.

II. FLUID APPROXIMATION

A. Basic equations

Assuming the ions to be at rest, thus providing a uniform neutralizing background, we describe the dynamics of the two electron counter-streaming populations in the fluid approximation by means of the two-fluid equations,

$$\frac{\partial \mathbf{p}_a}{\partial t} = -\mathbf{v}_a \cdot \boldsymbol{\nabla} \mathbf{p}_a - (\mathbf{E} + \mathbf{v}_a \times \mathbf{B}), \tag{1}$$

$$\frac{\partial n_a}{\partial t} = \boldsymbol{\nabla} \cdot \mathbf{j}_a, \tag{2}$$

$$\frac{\partial \mathbf{B}}{\partial t} = -\boldsymbol{\nabla} \times \mathbf{E}, \tag{3}$$

$$\frac{\partial \mathbf{E}}{\partial t} = \boldsymbol{\nabla} \times \mathbf{B} - \sum_a \mathbf{j}_a, \tag{4}$$

where

$$\mathbf{v}_a = \frac{\mathbf{p}_a}{(1+p_a^2)^{1/2}}, \quad \mathbf{j}_a = -n_a \mathbf{v}_a, \quad a = 1,2.$$

Here all quantities are normalized with a characteristic density $\bar{n}$, the speed of light c, and the plasma frequency $\omega_p = (4\pi \bar{n} e^2/m_e)^{1/2}$. Notice that the normalized electron skin depth is equal to 1.

In the following we limit our analysis to a magnetic field B_z generated by the Weibel instability with a single component along the z axis perpendicular to the plane of the initial streams and of the wave vector of the perturbation. Thus the electric field $\mathbf{E}$ is two dimensional and lies in the (x,y) plane.

We consider a homogeneous plasma in which at the initial time two uniform electron beams propagate in opposite directions along the x axis,

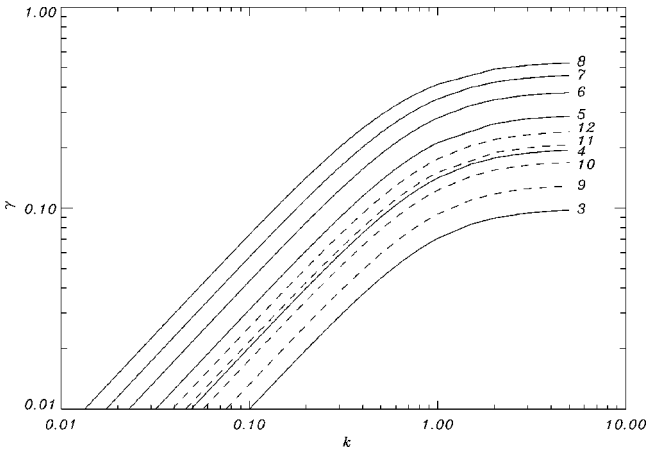

FIG. 1. The growth rate of the 1D Weibel instability in the symmetric (solid lines) and non-symmetric (dashed lines) case. The numbers refer to the runs as listed in Table I.

$$\mathbf{v}_1(t=0) = v_{0,1}\mathbf{e}_x, \quad \mathbf{v}_2(t=0) = -v_{0,2}\mathbf{e}_x, \tag{5}$$

with total current equal to zero. That provides a relationship between the beam densities:

$$n_{0,1} v_{0,1} = n_{0,2} v_{0,2}, \tag{6}$$

where the subscript zero indicates mean (zero order) quantities. We take a zero initial electric field and introduce a small magnetic perturbation with wave number k_0 along the y axis.

B. Linear dispersion equation

The general linear dispersion equation of the growing and propagating modes in a homogeneous plasma, obtained by linearizing the system of Eqs. (1)–(4), was given in [11]. Here we recall the dispersion equation of the growing Weibel mode in the one-dimensional (1D) nonrelativistic limit (see also [12]) which is needed in order to introduce the discussion of its nonlinear evolution and saturation:

$$\omega^2(1-\Omega_2^{-2})(1-\Omega_1^{-2}) - k_0^2[(1-\Omega_1^{-2})(1+\Omega_4^{-2}) + \Omega_3^{-4}] = 0, \tag{7}$$

where in the nonrelativistic limit, and keeping the notations of Ref. [11],

$$\Omega_1^{-2} = \Omega_2^{-2} = \sum_{a=1}^{2} \frac{n_{0,a}}{\omega^2},$$

$$\Omega_3^{-2} = \sum_{a=1}^{2} (-1)^{a+1} \frac{n_{0,a} v_{0,a}}{\omega^2}, \quad \Omega_4^{-2} = \sum_{a=1}^{2} \frac{n_{0,a} v_{0,a}^2}{\omega^2}. \tag{8}$$

In Fig. 1 we show the growth rate of the 1D Weibel instability vs the wave number k_0 for different nonrelativistic symmetric cases, $0.1 \leqslant v_{0,1} = v_{0,2} \leqslant 0.6$ (runs $3 \rightarrow 8$ in Table I), and nonsymmetric cases, $0.3 \leqslant v_{0,1} \leqslant 0.6$, $0.06 \leqslant v_{0,2} \leqslant 0.12$ (runs $9 \rightarrow 12$ in Table I).

The growth rate is larger for larger values of the stream velocity and increases linearly with k_0 for small values of k_0. The increase of the growth rate with k_0 saturates at $k_0 \simeq 1$,

corresponding to wavelengths of the order of the electron skin depth.

In the symmetric case, $v_{0,1}=v_{0,2}=v_0$, the growth rate expressed in dimensional units is equal to

$$\gamma \approx k_0 v_0, \tag{9}$$

in the long wavelength limit, $k_0 c/\omega_p \ll 1$, and to

$$\gamma \approx \frac{v_0}{c}\omega_p, \tag{10}$$

in the short wavelength limit, $k_0 c/\omega_p \gg 1$. Equations (9) and (10) are in agreement with the results obtained for a strongly anisotropic two-temperature Maxwellian distribution (see, e.g., Eq. (9.10.19) of Ref. [13]).

In the nonsymmetric case, $v_{0,1} \gg v_{0,2}$, we find

$$\gamma \approx k_0 v_{0,1}\left(\frac{n_{0,1}}{n}\right)^{1/2}, \tag{11}$$

in the long wavelength limit, and, in the short wavelength limit,

$$\gamma \approx \frac{v_{0,1}}{c}\omega_{p,1}, \tag{12}$$

where $\omega_{p,1}=(4\pi n_{0,1}e^2/m)^{1/2}$.

C. Nonlinear evolution of the Weibel instability

1. Analytical results

In the case of strongly asymmetric electron beams with $v_{0,1} \gg v_{0,2}$ and $n_{0,1} \ll n_{0,2}$, the ratio $\epsilon \equiv n_{0,1}/n_{0,2}$ can be used as a small expansion parameter in order to find approximate solutions of the nonlinear evolution of the Weibel instability in the nonrelativistic limit in the long wavelength regime, where the linear growth rate is linear in k_0, and in the short wavelength regime, where the linear growth rate is independent of k_0. These solutions allow us to identify basic features of the nonlinear evolution of the instability that are seen in the numerical result shown in Sec. IV. In finding these approximate solutions we follow the derivation presented in [12].

2. Long wavelength limit

First we consider a long wavelength perturbation, $k_0 c/\omega_p \ll 1$, in which case the growth rate is a linear function of the perturbation wave number [see Eqs. (9) and (11)]. We explore the nonlinear development of the instability in the phase before the increasingly small spatial scales mentioned in Sec. I are formed. In this limit we use the quasineutrality approximation

$$\sum_\alpha n_\alpha v_{x\alpha} \approx 0, \tag{13}$$

as suggested by the linear regime, and neglect the coupling to the transverse waves that are contained in the dispersion equation (7). Using the smallness of the parameter $\epsilon \equiv n_{0,1}/n_{0,2}$ and defining the variable $\kappa \equiv n_1/n_2 \ll 1$, we obtain

$$B_z \approx \frac{\partial \kappa}{\partial y}. \tag{14}$$

Then, the equations that describe the Weibel instability in the long wavelength limit are

$$\frac{\partial \kappa}{\partial t}+\frac{\partial \kappa u}{\partial y}=0, \tag{15}$$

$$\frac{\partial u}{\partial t}+u\frac{\partial u}{\partial y}=\frac{\partial \kappa}{\partial y}. \tag{16}$$

Here we have used the variables $u=v_{1y}/|v_{0x1}|$, and y and t are normalized on l and on $l/|v_{0x1}|$, respectively, with l the characteristic scale length along y. These equations have a form similar to that of the 1D gas dynamics equations, where, however, the pressure on the right hand side of Eq. (16) is proportional to minus the density κ. The velocity u can be written as the gradient of a potential ψ as

$$u=\frac{\partial \psi}{\partial y}, \tag{17}$$

which leads to the integral

$$\frac{\partial \psi}{\partial t}+\frac{u^2}{2}-\kappa=\text{const.} \tag{18}$$

Changing the independent variables x and t into u and κ, and introducing the auxiliary function

$$\chi=\psi-yu+t\left(\frac{u^2}{2}-\kappa\right), \tag{19}$$

such that

$$t=-\frac{\partial \chi}{\partial \kappa}, \quad \text{and} \quad y=ut-\frac{\partial \chi}{\partial u}, \tag{20}$$

we obtain

$$\frac{\partial y}{\partial u}=u\frac{\partial t}{\partial u}-\kappa\frac{\partial t}{\partial \kappa}, \tag{21}$$

$$\frac{\partial y}{\partial \kappa}=u\frac{\partial t}{\partial \kappa}+\frac{\partial t}{\partial u}, \tag{22}$$

and, eliminating y by cross differentiation and using Eq. (20),

$$\frac{\partial}{\partial \kappa}\left(\kappa\frac{\partial \chi}{\partial \kappa}\right)+\frac{\partial^2 \chi}{\partial u^2}=0. \tag{23}$$

By introducing the variable $\rho=2\kappa^{1/2}$, Eq. (23) can be reduced to the Laplace equation in the cylindrical coordinates ρ and u.

According to the theory of hydrodynamic-type instabilities in the long wavelength limit there are two generic types of nonlinear motions [14,15] the compression wave breaking and the rarefaction wave breaking.

The compression wave is described near the singularity by

$$\chi(u,\kappa)=a\ln\kappa+\frac{b}{(u^2+4\kappa)^{1/2}}, \tag{24}$$

which gives

$$t=-\frac{a}{\kappa}+\frac{2b}{(u^2+4\kappa)^{3/2}} \tag{25}$$

and

$$y=ut+\frac{bu}{(u^2+4\kappa)^{3/2}}. \tag{26}$$

For negative values of a and b, this solution describes the (local) increase and the steepening of the density of the faster and initially less numerous electrons that are pushed from large distances by a velocity that is odd in y. Their velocity increases as the time when the singularity occurs, $t=t_s$, is approached. For $t=t_s$, $\partial\kappa/\partial y$ and $\partial u/\partial y$ and B_z tend to infinity at finite κ and u. Due to quasineutrality, the velocity of the slow electron component is equal to κu. It describes the rarefaction in the slow electron density.

In Figs. 2(a), 2(b), and 2(c) the evolution of the fast component density and velocity and of the magnetic field, respectively, are shown for a case where the ratio a/b is small (and $t_s\approx 0$). According to Eq. (14) and the rules of implicit differentiation, the magnetic field is given by

$$B_z=\frac{1}{J}\frac{\partial t}{\partial u}, \tag{27}$$

where J is the Jacobian of the transformation from y,t to u,κ:

$$J=\left|\frac{\partial t}{\partial u}\frac{\partial y}{\partial \kappa}-\frac{\partial t}{\partial \kappa}\frac{\partial y}{\partial u}\right|. \tag{28}$$

We see the formation of the spike distribution in the electron density and the appearance of two spike structures in the velocity and magnetic field dependence on the y coordinate.

Choosing instead $\chi(u,\kappa)$ of the form

$$\chi(u,\kappa)=c\left[\left(\frac{\kappa^2}{2}-\kappa u^2\right)+\frac{u^4}{6}\right], \tag{29}$$

we obtain

$$t=c(u^2-\kappa), \tag{30}$$

$$y=ut-\tfrac{4}{3}cu^3. \tag{31}$$

For $c>0$ this solution describes the breakup of the faster electron population into two separate parts as shown in Fig. 3. The velocity and the density of this population around $y=0$ are given by $\kappa\approx(y/t)^2-t/c, u=-y/t$. At $t=0$, $y=0$, κ vanishes and takes the peaked form $\kappa=(3y/4c)^{2/3}-t/c, u=(3y/4c)^{1/3}$. The borders of the two parts of the separated electron population move as $y_{\pm}=\pm 4t^{3/2}/3c^{1/2}$ with velocity $u_{\pm}=\pm(t/c)^{1/2}$.

The validity of both solutions breaks down before the singularity in the electron density gradient described by Eqs. (25) and (26) and the density hole formation described by Eqs. (30) and (31) can reach their final stage. In particular, the time evolution of these solutions shows that small scales are formed, contrary to the long wavelength assumption. Nevertheless these solutions are instructive as they illustrate two of the main wave-break mechanisms in an unstable medium [15] the compressional break, Eqs. (25) and (26), and the rarefaction break, Eqs. (30) and (31). These structures are seen in the numerical solutions presented in the next section and persist beyond the region where the long wavelength approximation is valid.

3. Short wavelength limit

In order to follow the instability in the nonlinear regime where small scales have already formed, we now consider the short wavelength limit, when $k_0c/\omega_p\gg 1$. In this limit the growth rate does not depend on the perturbation wave number [see Eqs. (10) and (12)]. Using again the approximations that can be shown to be valid in the short wavelength limit in the linear phase of the instability, we neglect the displacement current, i.e., we disregard the coupling to the transverse waves. Furthermore, we restrict ourselves to a phase of the nonlinear development of the instability where the inequality $v_{0xa}>A_x$ still holds so that $v_{xa}\approx v_{0xa}$. Here A_x is the x component of the vector potential. Then we solve Eqs. (2) and (4) for n_a and obtain

$$\frac{\partial}{\partial t}(B_z-v_{x1,2}E_y)+v_{y2,1}\frac{\partial}{\partial y}(B_z-v_{x1,2}E_y)=-v_{x1,2}v_{y2,1}, \tag{32}$$

to be solved together with Eq. (1),

$$\frac{\partial v_{y1,2}}{\partial t}+v_{y1,2}\frac{\partial v_{y1,2}}{\partial y}=-(E_y-v_{y1,2}B_z). \tag{33}$$

Introducing the Lagrangian derivatives

$$d/dt_{1,2}\equiv\partial/\partial t+v_{y1,2}\partial/\partial y,$$

we obtain from Eqs. (32), (33) the following equations:

$$\frac{d^2}{dt_{1,2}^2}B_z+v_{x1}v_{x2}B_z-v_{x2,1}\left(\frac{d^2}{dt_{1,2}^2}+1\right)E_y=0, \tag{34}$$

which describe the nonlinear evolution of the coupled Langmuir waves and Weibel instability in the nonrelativistic, short wavelength limit. For $n_{0,1}\ll n_{0,2}$, we expand Eq. (34) in powers of $\epsilon\equiv n_{0,1}/n_{0,2}=v_{x2}/v_{x1}$. We find that, to leading order in ϵ, Eq. (34) factorizes into modes with $d/dt\sim O(\epsilon^0)$, corresponding to nonlinear Langmuir waves, and into modes with $d/dt\sim\mathcal{O}(\epsilon^{1/2})$, corresponding to nonlinear Weibel modes. The latter are given by

$$\frac{d^2}{dt_1^2}B_z+v_{x1}v_{x2}B_z-v_{x2}E_y=0, \quad \text{and} \quad v_{x1}E_y=0. \tag{35}$$

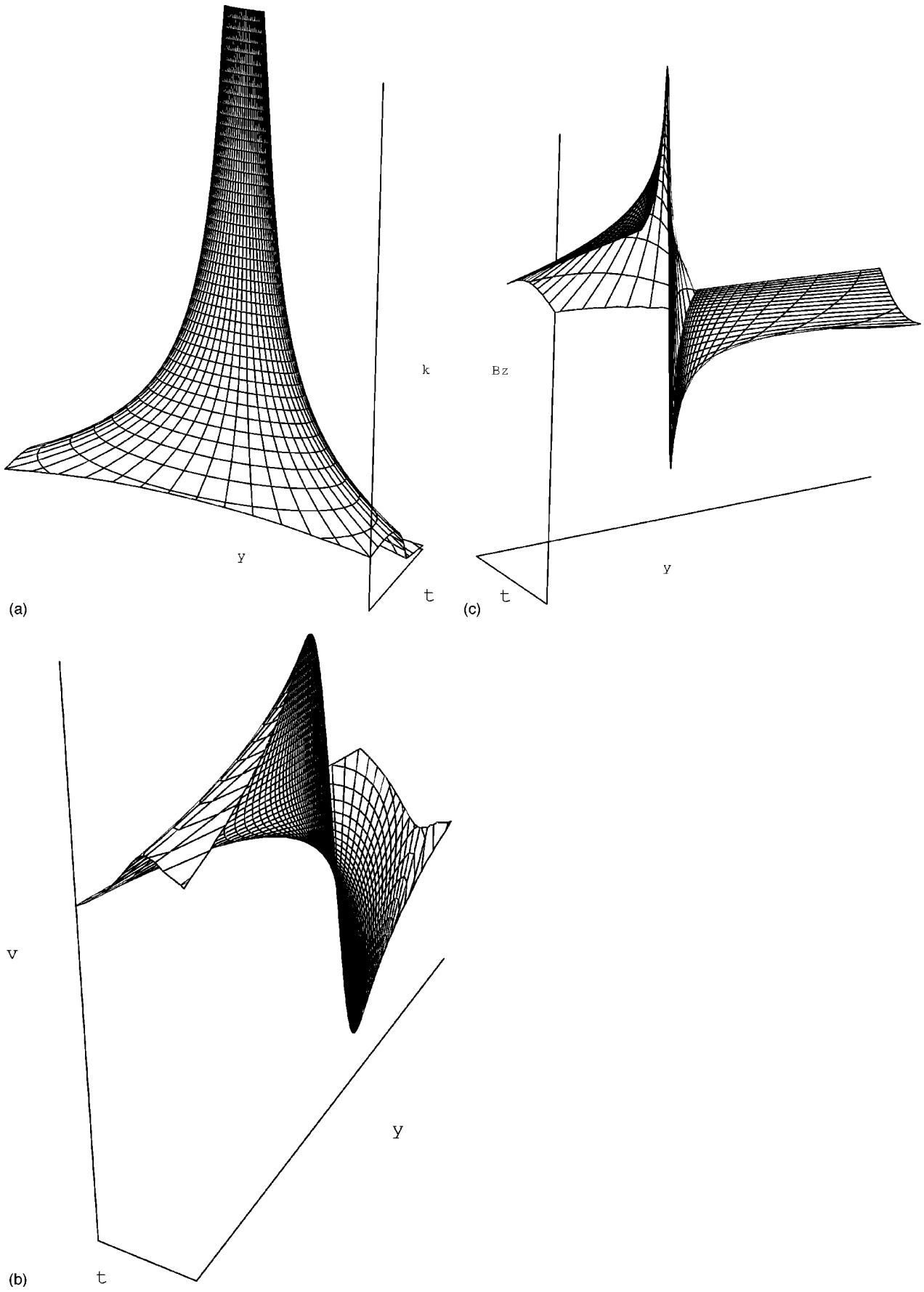

FIG. 2. Compression of the faster electron component: (a) density ratio κ, (b) velocity v, and (c) magnetic field B_z vs t and y; y runs from -3 to 3 and t from 0 to -2. In (a) $t=-2$ corresponds to the front of the figure and $t=0$ to the back; in (b) and (c) $t=-2$ corresponds to the back and $t=0$ to the front.

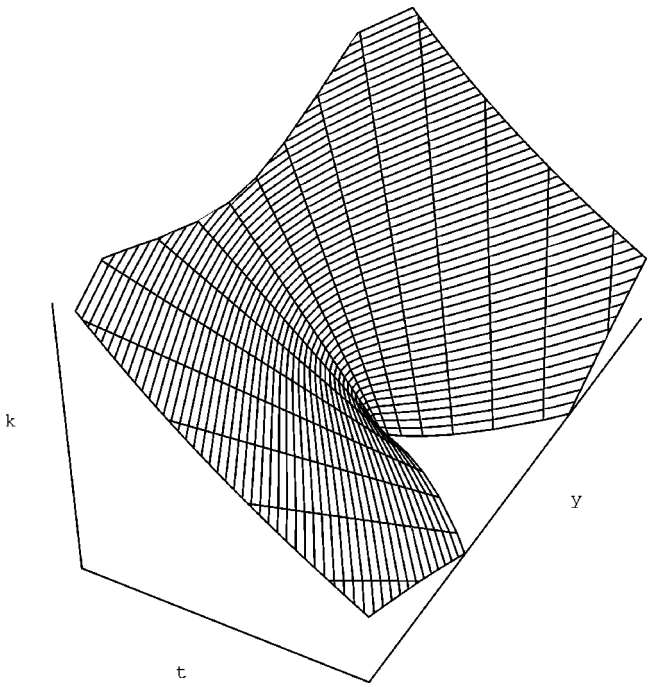

FIG. 3. Evolution of the density ratio κ of the faster electron component when it breaks into two pieces vs t and y; y runs from -3 to 3 and t from -2 (back) to 2 (front).

This factorization holds as long as $d/dt_{1,2}$ can be ordered in the same way in powers of $\epsilon^{1/2}$. Equations (35) indicate that in this regime the nonlinear evolution of the Weibel instability remains approximately quasineutral and has an exponential behavior in the Lagrangian variable of the faster electron fluid. Conversely, the nonlinear evolution of the Langmuir waves remains harmonic in the Lagrangian variable of the slower, more numerous, electron fluid.

By transforming the above solution back from Lagrangian to Eulerian variables, we see that Eqs. (35) predict the formation of a single cusp in the density of the fast electron component per wavelength of the initial perturbation. This singularity arises in a finite time $t_s \sim \gamma^{-1} \ln(k_0 \xi_0)$, that depends logarithmically on the amplitude of the initial displacement ξ_0.

When κ becomes sufficiently large, the quasineutrality approximation is no longer valid, which leads to the increase of the y component of the electric field. A direct perturbative calculation shows that the difference between d/dt_1 and d/dt_2 causes the electrostatic field E_y, and thus the coupling term $\omega_{pe}^2 v_{x2} E_y$ in the first of Eqs. (35), to grow faster than the magnetic field B_z. This can be seen analytically by computing $d/dt_2 - d/dt_1$ and by using the following relationship between the Lagrangian coordinates $y_{0,1}$ and $y_{0,2}$ of the two electron fluids that correspond to the same Eulerian position y at time t,

$$y_{0,1} = y_{0,2} + \frac{B_z(y_{0,1}, t)}{\Delta} \tag{36}$$

with $\Delta \equiv (v_{x2} - v_{x1})/v_{x2} v_{x1}$. This relationship is obtained by integrating Eqs. (32) in time and by combining them so as to eliminate E_y. The faster growth of E_y indicates that charge separation cannot be neglected as the time t_s is approached when the factorization between the Weibel instability and the Langmuir waves ceases to be valid. The resulting coupling between the Weibel instability and the Langmuir modes leads to the generation of small scale patterns. However, this effect does not prevent the wave break as it is seen in the results presented in the following subsection.

D. Numerical results

In order to study the nonlinear evolution of the Weibel instability in the fluid approximation, we integrate Eqs. (1)–(4) numerically in the interval $L_y = 2\pi/k_0$ with initial conditions given by Eq. (5) for the electron stream velocities and by

$$\mathbf{E}(t=0) = \mathbf{0}, \quad \mathbf{B}(t=0) = b \sin(k_0 y) \mathbf{e}_z, \tag{37}$$

for initial electric and magnetic field. The perturbation amplitude b is equal to 10^{-3}.

The numerical code runs on massively parallel computers (CM200 and CM5); the details of the algorithm are given in Ref. [11].

Characteristic values of the electron beam velocities lie in the range $[0.1c, 0.6c]$ (where c is the speed of light), which are relevant for laser-plasma applications. At higher values relativistic effects should be taken into account. This nonrelativistic range is chosen because of the present limitation of the Vlasov code adopted (see Sec. III), but it is expected that the saturation mechanism will not be qualitatively changed in a relativistic plasma.

In Fig. 4 we show the results of a symmetric run (run 1 in Table I) made by using the initial conditions of Eqs. (5)–(37) with the following parameters: $v_{0,1} = v_{0,2} = 0.3$, $n_{0,1} = n_{0,2} = 0.5$, and $k_0 = 0.2$. In this figure we plot the magnetic field B_z, the y component of the electric field, and the densities of the two electron populations vs y at $t = 60$, 70, 72.

For $t \leqslant 60$ (linear phase) the amplitude of the magnetic field grows exponentially with growth rate $\gamma = 0.06$. The perturbation does not propagate, in agreement with the normal mode analysis which yields zero frequency ($\mathrm{Re}(\omega) = 0$) for this mode. At $t = 60$ the wave number of the perturbation is equal to its initial value which corresponds to the largest wavelength admitted by the system (see Fig. 4 dashed lines).

For $t > 60$ the amplitude of the velocity perturbations becomes comparable to that of the two initial streams and the nonlinear terms become important. During this phase (see Fig. 4, continuous lines) higher and higher spatial harmonics are produced in the regions close to the maxima and minima of the magnetic field. In these regions, the spatial structure of the magnetic field has a typical cusplike form and very large density spikes are produced. From the last two frames of Fig. 4 we see that the two electron populations are concentrated around the peaks of the magnetic field, on opposite sides at each peak. Each of the two electron populations develops two spikes. In Fig. 4 we also show that an electrostatic field E_y is generated by the coupling of the instability to plasma waves. This coupling is nonlinear since in the linear nonrelativistic case the electrostatic field E_y is decoupled from the other fields. It is also seen that E_y grows faster, and eventually becomes larger than B_z. Close to the time when the singularities appear, the electrostatic part of the Lorentz force in the y direction is dominant over the magnetic part.

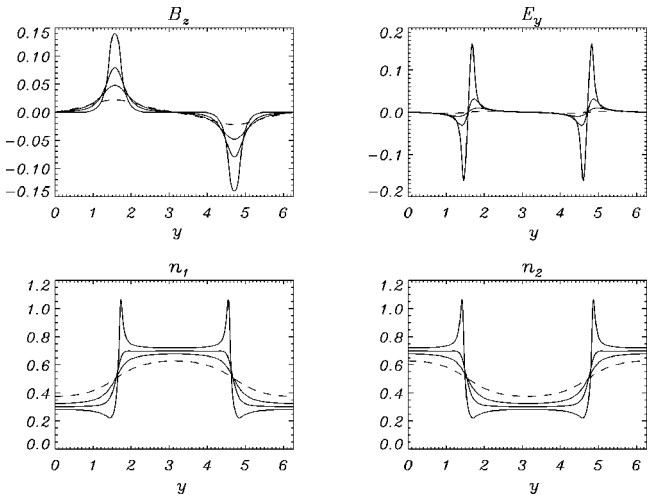

FIG. 4. The formation of the singularity in a symmetric case (run 1 in Table I). In the four frames we show the magnetic field, the y component of the electric field, and the densities of the two electron populations as a function of y at the end of the linear phase $t=60$ (dashed lines) and during the nonlinear evolution $t=70,72$ (solid lines).

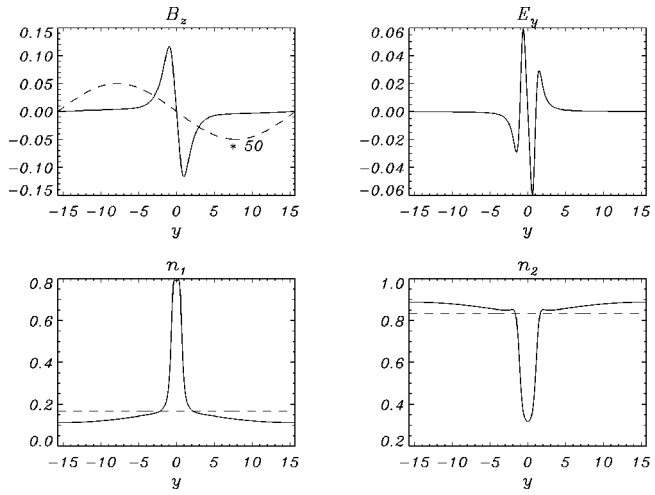

FIG. 5. The formation of the singularity in a nonsymmetric case (run 2 in Table I). In the four frames we show the magnetic field, the y component of the electric field, and the densities of the two electron populations as a function of y at the end of the linear phase $t=70$ (dashed lines) and during the nonlinear phase $t=80$ (solid lines).

In the case of two initially nonsymmetric beams, which is the more interesting case for laser plasma applications, the location and the spatial structure of the breaking are different from those seen in the symmetric case. In the initial phase each of the two electron populations develops a single structure of the density per initial wavelength and the ratio $\kappa \equiv n_1/n_2$ peaks at the center as discussed in Sec. II C 2 below Eq. (24) and illustrated in Fig. 5. The resulting magnetic field B_z has an overall dipolar structure with a central current separating the two polarities carried by the faster electron population and two external return currents carried by the slower electrons.

Later in time, when $t \approx t_s$, the electrostatic field E_y increases faster than B_z, in agreement with the results of Sec. II C 3 and, when two cusps are formed, the electric part of the Lorentz force in the y direction becomes dominant over the magnetic part. In a number of runs not reported here, except for run 2 in Table I, we have found that the peaks of the magnetic field (as well as of the other quantities) move closer to each other when the ratio of $v_{0,1}/v_{0,2}$ increases and that the splitting of the density peak in each of the two electron populations into two closely spaced cusps occurs for later and later times. In Fig. 5 we show the results of a non-symmetric run with growth rate $\gamma=0.04$ (run 2 in Table I) obtained by using the following initial parameters: $v_{0,1}=0.5$, $v_{0,2}=0.1$, $n_{0,1}=0.1\overline{6}$, and $n_{0,2}=0.8\overline{3}$. We plot the same fields as in the symmetric case at the end of the linear phase (dashed lines) and during the nonlinear phase (continuous lines).

The results of these fluid simulations show that the nonlinear effects do not saturate the perturbation growth. Moreover, they are responsible for the formation of the spikes that occur on a very short time scale $O(1)$ regardless of the initial conditions. Actually, there is no process in the model (the fluids are ideal) capable of saturating the growth of the spikes. This is seen in the simulations as a numerical divergence that occurs roughly at the same time regardless of the mesh size, suggesting also that a singularity is forming in a finite time.

III. KINETIC EVOLUTION

In this section we investigate the role of the kinetic effects after the time of the formation of the singularities found in the two electron-fluid description.

The linear theory of the Weibel instability of an anisotropic electron population with thermal velocities $v_{\mathrm{the1}} > v_{\mathrm{the2}}$ in an unmagnetized plasma was studied in a kinetic description in [16]. For a geometry corresponding to that of the present paper, the stability condition of the purely growing mode was found to be

$$k_y^2 \geqslant \frac{v_{\mathrm{the1}}^2}{v_{\mathrm{the2}}^2} - 1. \tag{38}$$

This condition shows that thermal effects, not included in the analysis in the previous sections, tend to stabilize short wavelength modes first, which are the most unstable in the fluid approximation. In [17], the quasilinear mode stabilization was studied in the limit of small anisotropy and was shown to lead to the isotropization on the distribution function and to the transformation of kinetic energy into magnetic energy. In [18], different types of transverse electromagnetic (e.m.) instabilities are studied analytically using a quasilinear approximation of the Vlasov-Maxwell equations. The results are then tested by numerical particle simulations. In particular, two independent energy constants are given that remain such even when a significant fraction of the initial kinetic energy anisotropy is transferred into magnetic energy. Furthermore, the authors show that the instability saturates when the bounce frequency of the electrons trapped by the magnetic field generated by the instability [see [18], Eq. (71)] becomes comparable to the instability growth rate,

$$\gamma \simeq \omega_B \equiv \left| \frac{ek}{m} \frac{vB}{c} \right|^{1/2}. \tag{39}$$

The kinetic behavior of a collisionless plasma is described by the Vlasov equation that follows the evolution of the plasma particle distribution function in phase space under the action of the e.m. fields. The time evolution of the distribution function changes the plasma currents, and the Vlasov equation must be coupled to Maxwell's equations in order to have a self-consistent description of the system. These equations are integrated numerically in the 2D (x,y) $3V$ (v_x,v_y,v_z) phase space by using a ''Vlasov-Maxwell'' code including the magnetic term in the Lorentz force. The code has been tested in several different cases (Langmuir waves, Bernstein waves, Landau damping, and two-stream instability) and runs presently on the Cray T3D-T3E supercomputer. For the problem under consideration we restrict ourselves to a 1D $2V$ phase space (y,v_x,v_y).

A. Equations

We normalize the Vlasov-Maxwell equations on the same characteristic quantities used in the fluid approximation (see Sec. II A): the electron mass m_e, a characteristic particle density $\overline{n}$, the speed of light c, the electron plasma frequency $\omega_p=(4\pi \overline{n} e^2/m_e)^{1/2}$, and the characteristic electric and magnetic fields $\overline{E}=\overline{B}=-mc\omega_p/e$. Then, the dimensionless equations read

$$\frac{\partial f}{\partial t}+\mathbf{v}\cdot\frac{\partial f}{\partial \mathbf{x}}+(\mathbf{E}+\mathbf{v}\times\mathbf{B})\frac{\partial f}{\partial \mathbf{v}}=0, \tag{40}$$

$$\frac{\partial \mathbf{E}}{\partial t}=\nabla\times\mathbf{B}-\mathbf{J}, \tag{41}$$

$$\frac{\partial \mathbf{B}}{\partial t}=-\nabla\times\mathbf{E}. \tag{42}$$

As in the fluid approximation (see Sec. II), we limit our study to a magnetic field B_z with a single component along the z axis and to a 2D electric field $\mathbf{E}=(E_x,E_y)$.

Given the distribution function $f(y,v_x,v_y)$ in phase space with $0\leqslant y\leqslant L_y$, we define, in dimensionless form, the mean particle density and velocity as

$$n(y,t)=\int_{-\infty}^{\infty} f(y,v_x,v_y)dv_x dv_y, \tag{43}$$

$$\langle \mathbf{v}\rangle(y,t)=-\frac{\mathbf{J}}{n}=\frac{1}{n}\int_{-\infty}^{\infty} f(y,v_x,v_y)\mathbf{v}dv_x dv_y, \tag{44}$$

and the mean kinetic energy as

$$E_k(t)=\frac{1}{L_y}\frac{1}{2}\int_0^{L_y}(\epsilon_x+\epsilon_y)dy, \tag{45}$$

where

$$\begin{Bmatrix}\epsilon_x\\ \epsilon_y\end{Bmatrix}(y,t)=\int_{-\infty}^{\infty} f(x,v_x,v_y)\times\begin{Bmatrix}v_x^2\\ v_y^2\end{Bmatrix}dv_x dv_y. \tag{46}$$

Finally, the mean electric and magnetic energies are given by

$$E_e(t)=\frac{1}{L_y}\frac{1}{2}\int_0^{L_y}(E_x^2+E_y^2)dy, \quad E_m(t)=\frac{1}{L_y}\frac{1}{2}\int_0^{L_y}B_z^2 dy. \tag{47}$$

B. Kinetic simulations

Equations (40)–(42) are integrated in the phase space (y,v_x,v_y) with the following initial conditions:

$$f(v_x,v_y)=\frac{1}{\pi\beta}e^{-v_y^2/\beta}[\,\delta e^{-(v_x-v_{0,1})^2/\beta} + (1-\delta)e^{-(v_x-v_{0,2})^2/\beta}], \tag{48}$$

$$E_x=E_y=0, \quad B_z=b\sin(k_0 y), \tag{49}$$

where $\beta^{1/2}$ is the thermal velocity and δ is a parameter measuring the symmetry of the electron beams ($\delta=0.5$ in the symmetric case) and $b=10^{-3}$. Note that the initial particle density is uniform and equal to one, $\langle n\rangle(y,t=0)=1$. From Eq.(48) we obtain

$$\epsilon_x(t=0)=\frac{\beta}{2}+\delta v_{0,1}^2+(1-\delta)v_{0,2}^2, \quad \epsilon_y(t=0)=\frac{\beta}{2}. \tag{50}$$

In Table I we present the results of a number of ''kinetic'' runs with a typical numerical mesh size of $128\times140\times140$ points. All these runs are performed with $\beta=0.01$, $L_y=2\pi/k_0$, and $0\leqslant t\leqslant200$. The value of β has been chosen small for consistency with the fluid regimes considered in the previous sections. Thermal effects are important in the linear phase only in runs 3 and 9. In Table I we list, from left to right, the number of the run, the wave number k_0 of the

TABLE I. Results of a number of ''kinetic'' runs: the number of the run, wave number k_0, initial mean velocities of the two electron streams, $v_{0,1}$ and $v_{0,2}$, kinetic energy E_k^0, linear fluid growth rate $\gamma_{\rm fluid}$, kinetic linear growth rate $\gamma_{\rm kin}$, minimum value $\rho_e^{\rm min}$ of the gyroradius ρ_e, and efficiency η.

Run	k_0	$v_{0,1}$	$v_{0,2}$	E_k^0	$\gamma_{\rm fluid}$	$\gamma_{\rm kin}$	$\varrho_e^{\rm min}$	η
1	0.2	0.3	0.3	0.05	0.06	0.06	1.7	0.1
2	0.2	0.5	0.1	0.03	0.04	0.04	1.2	0.04
3	1.0	0.1	0.1	0.01	0.07	0.02	4.5	0.01
4	1.0	0.2	0.2	0.025	0.14	0.10	1.5	0.12
5	1.0	0.3	0.3	0.05	0.21	0.18	1.2	0.16
6	1.0	0.4	0.4	0.085	0.28	0.25	1.1	0.26
7	1.0	0.5	0.5	0.13	0.35	0.32	1.4	0.38
8	1.0	0.6	0.6	0.185	0.41	0.41	1.2	0.5
9	1.0	0.3	0.06	0.014	0.09	0.05	1.2	0.03
10	1.0	0.4	0.08	0.021	0.12	0.09	1.1	0.05
11	1.0	0.5	0.1	0.03	0.15	0.12	1.1	0.06
12	1.0	0.6	0.12	0.041	0.17	0.16	1.5	0.07

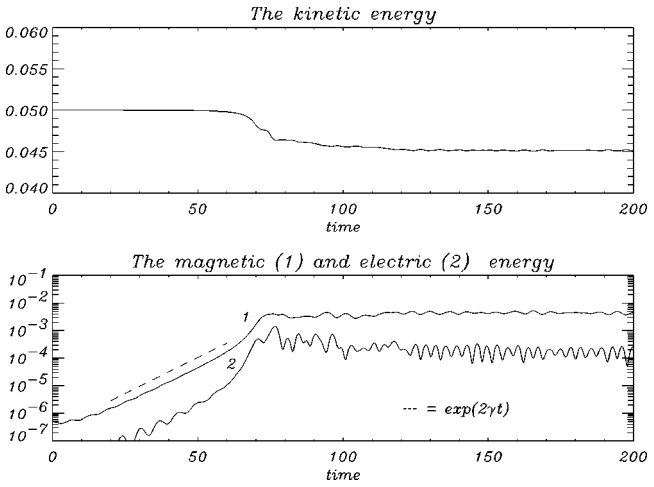

FIG. 6. The time evolution of the kinetic, magnetic and electric energies for run 1.

initial perturbation, the initial mean velocities of the two electron streams $v_{0,1}$ and $v_{0,2}$, the kinetic energy E_k^0 at $t=0$, the linear fluid growth rate γ_{fluid}, the kinetic linear growth rate γ_{kin}, the minimum value $\varrho_e^{\min}$ of the gyroradius $\varrho_e(t)$ and finally the efficiency $\eta=\max[E_m(t)/E_k^0]$. We define the reference electron gyroradius as the ratio between the smaller initial velocity of the streams and the maximum value (in space) of the magnetic field,

$$\varrho_e(t)=\frac{\min(v_{0,1},v_{0,2})}{\max[B(y,t)]}. \tag{51}$$

This reference value measures the strength of the magnetic field B_z and the characteristic size of the electron orbits.

The fluid growth rate γ_{fluid} is obtained by solving the linear dispersion equation of Eq. (7) and the kinetic growth rate γ_{kin} is calculated by making, during the linear phase, a best fit of the curve $[E_m(t)]^{1/2}$. In the nonsymmetric runs 2 and 9→12, we have fixed the ratio between the two beam velocities, $v_{0,2}=0.2\ v_{0,1}$. Therefore, by requiring that the total initial current is zero, we obtain $\delta=0.1\overline{6}$ (i.e., $n_{0,1}=0.1\overline{6}$, $n_{0,2}=0.8\overline{3}$), while in the symmetric case $\delta=0.5$ (i.e., $n_{0,1}=n_{0,2}=0.5$).

C. The kinetic Weibel instability

In the first two runs (see Table I) we consider two initially symmetric beams with mean opposite velocities $v_{0,1}=v_{0,2}=0.3$ and two nonsymmetric beams of velocities $v_{0,1}=0.5$, $v_{0,2}=0.1$. The beams are perturbed by an initial sinusoidal perturbation of wave number $k_0=0.2$, see Eqs. (48) and (49). These cases, except for the nonzero temperature ($\beta=0.01$), are analogous to the two fluid runs described in Sec. II D.

In Fig. 6 we show the time evolution of the kinetic $E_k(t)$, magnetic $E_m(t)$ and electric $E_e(t)$ energies for run 1. After a rapid transient, $t<10$, the magnetic energy starts to grow exponentially with two times the growth rate of the mode amplitude as obtained from the fluid homogeneous dispersion relation. This agreement is not surprising since the wavelength of the perturbation is much larger than d_e and $k_0^{-1}\gamma$ is much greater than the thermal velocity. During this phase, the magnetic field $B_z(y)$ grows with a constant phase (i.e., without propagation in the y direction) as expected from the fluid analysis.

For $t\sim 60$ nonlinear effects become important and the wave, as observed in the fluid approximation (see Sec. II D), starts to deform and to generate smaller and smaller spatial scales. As a result, the instability speeds up since for $k_0\leqslant k\leqslant 1$ the growth rate increases linearly with k (see Sec. II B).

For longer times, $t\geqslant 70$, kinetic effects come into play and the instability saturates. The magnetic energy E_m becomes statistically constant, while the electric energy E_e reaches its maximum value at saturation and then starts to decrease. This is in agreement with the fact that as soon as the instability saturates and the growth rate decreases, the wave becomes dominated by the magnetic field, as is the case for low frequency e.m. waves.

The wave distortion and the saturation in the kinetic regime are illustrated in Fig. 7 where we plot the magnetic field B_z at times $t=40,70,100$, and its Fourier spectrum $B_{z,k}$ at $t=100$ (left hand side) as well as ϵ_x, ϵ_y, n, and E_y at $t=100$ (right hand side) for run 1. The star in the bottom left hand frame represents the wavenumber of the initial perturbation. Notice that ϵ_x and ϵ_y are spatially constant at $t=0$.

Figure 7 shows that the initial large scale perturbation ($k=0.2$), which is amplified but not deformed during the linear phase, peaks in the same points as in the symmetric fluid case (see Fig. 4). In particular two peaks per wavelength are seen in each electron population. This correspondence between the number and location of the density peaks in the fluid and in the kinetic description is also observed in the asymmetric run 2 not shown here.

This process generates larger and larger wave numbers $k\gg k_0$, as in the fluid case. In addition it causes the electron velocities in phase space to rotate around the peaks of the magnetic field, in agreement with the magnetic trapping mechanism discussed in [18]. The distribution function in the v_y direction widens until it acquires a velocity spread of the order of the initial beam velocity anisotropy along v_x. This effective isotropization of the electron distribution function combined with the increase of the wave number leads to the mode stabilization, consistent with the linear stability condition given by Eq. (38). The electron gyroradius ϱ_e defined by Eq. (51) decreases and eventually both $\lambda\equiv 2\pi/k$ and ϱ_e become of the same order and comparable to d_e (in dimensionless units $d_e=1$). The small scale generation process stops and the instability saturates. Indeed, the next picture at a later time ($t=100$) shows that the perturbation has the same spatial scale as in the previous one at $t=70$, while in the fluid case numerical divergence was observed at $t\simeq 72$. In the bottom left hand frame of Fig. 7 we show the Fourier spectrum of the magnetic field at $t=100$. We see that, in the range $k_0\leqslant k<2\pi/d_e$, the excitation of the nonlinear higher spatial harmonics has generated a power law spectrum that decreases exponentially for larger wave numbers; the same exponential cut-off is observed in the spectra of all other quantities. In the first two frames on the right hand side of Fig. 7 we see that ϵ_y, which was initially negligible with respect to ϵ_x, becomes nearly comparable to ϵ_x. Both quantities peak in the same points of the magnetic field. The electron density, see next picture, is spatially concentrated in this region. In the last frame we show the electrostatic field

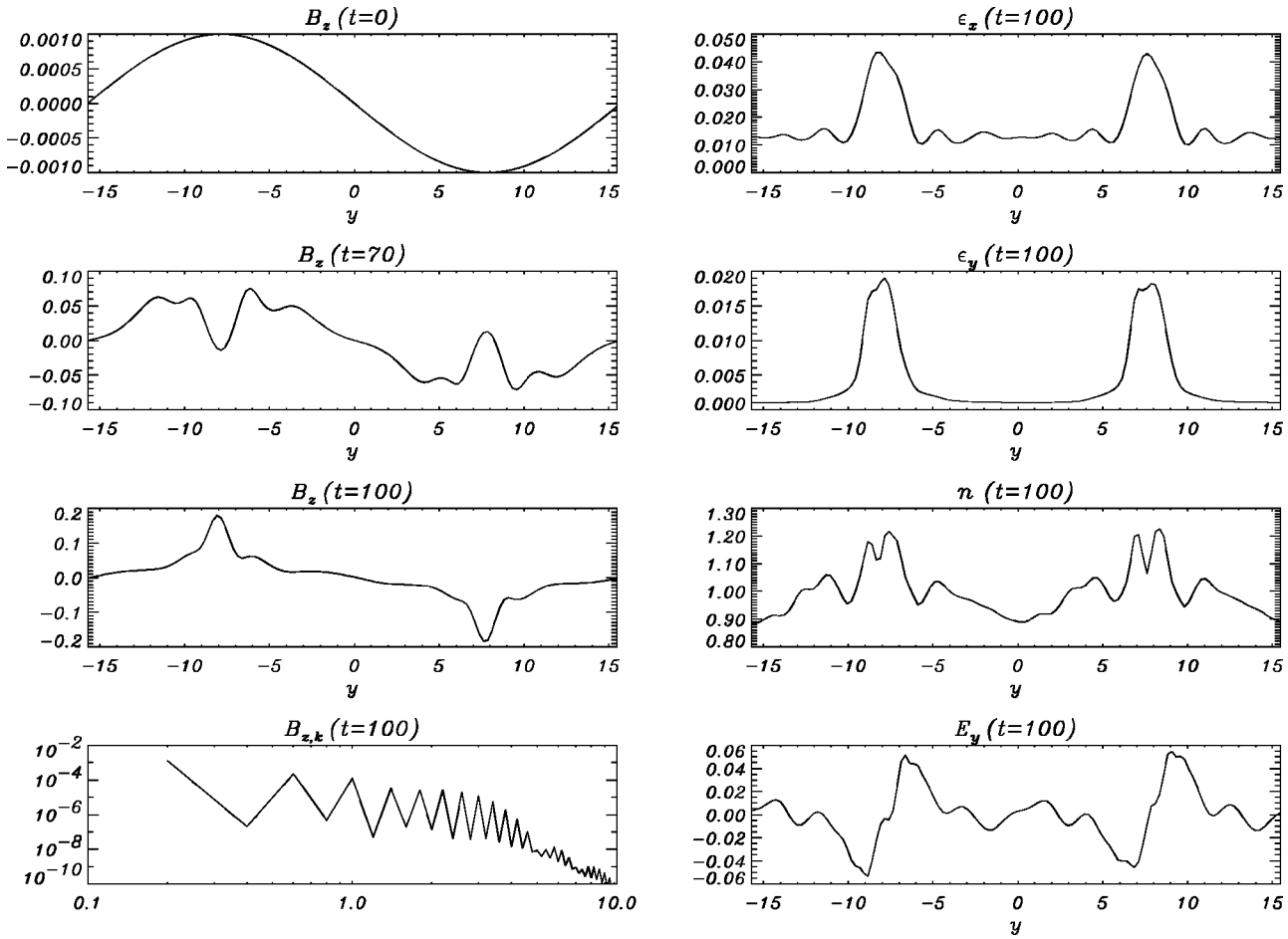

FIG. 7. The magnetic field B_z (left hand side) vs y at $t=40,70,100$, its Fourier spectrum $B_{z,k}$ at $t=100$, and (right hand side) ϵ_x, ϵ_y, n and E_y at $t=100$. The star in the bottom left hand frame is the wave number ($k_0=0.2$) of the initial perturbation.

E_y perpendicular to the initial beam direction that, as in the fluid case (see Fig. 4), results from nonlinear interactions.

The saturation condition discussed here requires that both the perturbation wavelength λ and the electron gyroradius ϱ_e become comparable to the electron skin depth d_e. This condition is equivalent to that discussed in [18], which requires $\gamma \simeq \omega_B$. In fact, by using Eq. (10), Eq. (39) can be rewritten as $\varrho_e/d_e = kd_e$.

The time evolution of the electron distribution function, the rotation of the beams around the magnetic field B_z and the spread in the direction perpendicular to the initial beams are shown for the parameters of run 6 in Figs. 8–10. In Fig. 8 the contour line of the electron distribution function at $y=0.5$ in the (v_x, v_y) plane are shown at three different times. Notice that the two beams spread in v_y, reduce their difference in v_x, and become spatially separated. This is shown by the shrinking of the portion of the distribution that corresponds to negative v_x velocities. A complementary situation, where the portion of the distribution that corresponds to positive v_x velocities shrinks, is seen at $y=3.6$ in the last frame. This evolution of the distribution function is also seen in Figs. 9 and 10 where the isocontour corresponding to 0.6 of the maximum value of the distribution function is shown in a 3D perspective as a function of y, v_x, and v_y. By comparing the isocontour of the initial beams, the two straight cylinders in each figure, with the isocontours at $t=25$, Fig. 9, and $t=55$, Fig. 10, we see a y-dependent rotation of the velocities in Fig. 9 followed by the beam separation in y in Fig. 10.

In runs 3–12 we study the efficiency of the Weibel instability in generating magnetic energy by varying the intensity of the two initial electron beams in the symmetric as well as in the nonsymmetric case. In order to save computational resources without losing the main physical effects observed in runs 1 and 2, we start the simulations with a larger initial

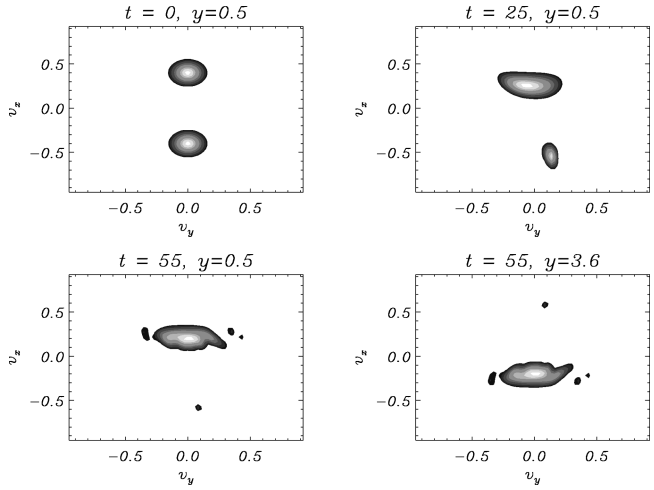

FIG. 8. Shaded isocontours of the distribution function $f(v_x, v_y)$ at $y=0.5$ (first three frames) and $y=3.6$ (last frame) at times $t=0,25,55,55$, respectively. The parameters are those of run 6.

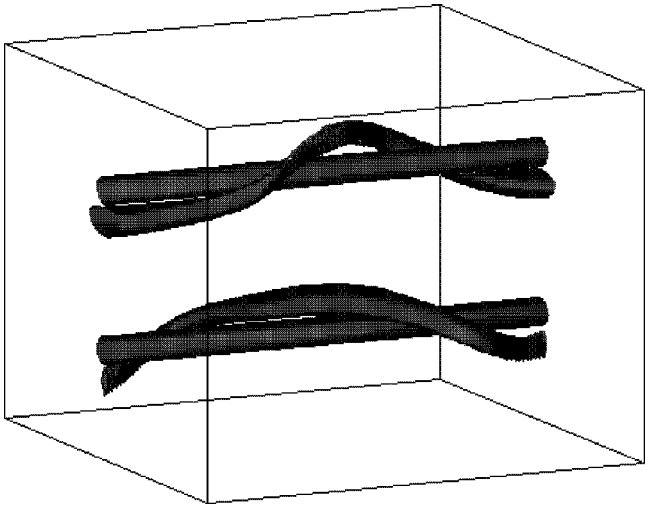

FIG. 9. Isocontours of the distribution function $f(y,v_x,v_y)$ at times $t=0$ (straight cylinders) and $t=25$ (bending cylinders). Periodic boundary conditions are used in the y direction (i.e., in the direction of the cylinders). The v_x and v_y directions are the vertical and the depth directions, respectively. The parameters are those of run 6.

wave number, $k_0=1$, which in the fluid approximation lies in the most unstable range (see Fig. 1). In the cases where the thermal velocity turns out to be comparable to γ/k_0, the kinetic growth rate $\gamma_{\rm kin}$ is significantly reduced with respect to the fluid one $\gamma_{\rm fluid}$ (see Table I). Clearly, this thermal stabilizing effect is more important for small values of the beam velocities.

In Fig. 11 we show the magnetic E_m energy and the efficiency η vs time, respectively. Note that an efficiency $\eta=0.5$ corresponds to complete equipartition of the initial kinetic energy into kinetic and magnetic energy.

First of all, we observe that the efficiency of the Weibel instability is enhanced when the two initial streams are symmetric. For example, the symmetric runs 4 and 5 have a lower or comparable growth rate with respect to the nonsymmetric runs 11 and 12, while their efficiency is larger. This is

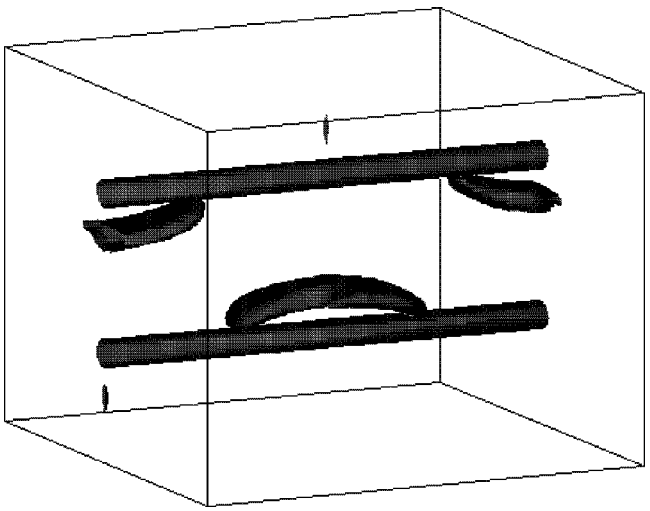

FIG. 10. The isocontours of the distribution function $f(y,v_x,v_y)$ as in Fig. 9, but at times $t=0$ (straight cylinders) and $t=55$ (pancakes). The parameters are those of run 6.

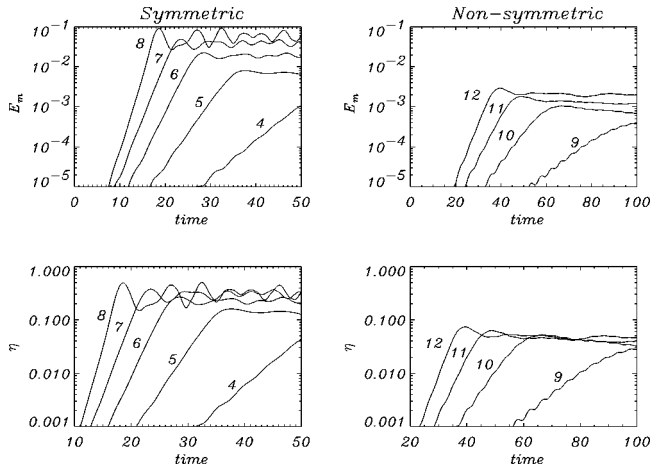

FIG. 11. The time evolution of the magnetic energy E_m and of the efficiency η for different symmetric (left hand side) and nonsymmetric (right hand side) runs. The numbers correspond to the number of the run as given in Table I.

directly related to the saturation mechanism of the instability. In the nonsymmetric case, as soon as the magnetic field becomes strong enough to make the gyroradius of the electrons of the slow beam of the order of the electron skin depth, i.e., as soon as the spreading in the v_y direction is comparable with $v_{0,2}$, the instability saturates. However, at this stage the gyroradius of the electrons of the fast beam is greater than the electron skin depth (in our case five times greater) since $v_{0,1}>v_{0,2}$. As a result, most of the kinetic energy stored into the ''fast'' beam is not converted into magnetic energy as in the symmetric case.

The efficiency increases, both in the symmetric and nonsymmetric cases, when the growth rate of the instability is larger.

Finally, the evolution of the minimum gyroradius ϱ_e vs time as defined in Sec. III B shows that in all runs (except for run 3) saturation occurs as soon as the gyroradius becomes $O(1)$ (and comparable to the electron skin depth) regardless of the initial conditions (beam velocities, wave number). After this time, in all cases, the gyroradius remains constant in time. In the case of run 3, which is characterized by a small growth rate, the duration of the simulation ($t_{\rm fin}=200$) is not long enough to produce a gyroradius of order 1. Notice that in the nonsymmetric case, where $v_{0,1}=5v_{0.2}$, the minimum gyroradius of the faster beam lies in the range $[5<\varrho_e^{\rm min}<10]$, larger than d_e.

IV. CONCLUSIONS

We have studied the fluid and the kinetic nonlinear evolution of the Weibel instability in the case of two initially uniform nonrelativistic beams of electrons streaming in opposite directions. The beams are perturbed by a small transversal disturbance of wavelength greater or comparable to the electron skin depth d_e.

In the linear phase, the Weibel instability grows exponentially with a null phase velocity. In this phase, a magnetic field perpendicular to the plane of the beams and of the perturbation is generated.

Using a fluid approximation for each of the two electron populations, we show that during the nonlinear evolution,

singularities form at finite times. This process may be understood as the breaking of the unstable waves. In the long wavelength limit two spikes per perturbation wavelength form in the magnetic field, in the velocity and in the density of each of the two electron populations. The location and time development of these structures depend on whether the two initial beams are symmetric or not. In the symmetric case the two spikes form, respectively, at the maximum and at the minimum of the initial perturbation. As the initial beam asymmetry is increased, the two developing spikes form closer to each other. In the strong nonsymmetric case, in the initial phase, a single structure is seen in the density. Eventually, as the time when the singularity forms is approached, this structure develops two distinct but closely spaced spikes. During the spike formation, larger and larger gradients are generated and, since in the fluid approximation the plasma is assumed to be collisionless, the small scale generation cannot be stopped. As a result scales comparable or shorter than the characteristic kinetic scales (such as the electron gyroradius) are formed in a few (normalized) times and the fluid approximation becomes meaningless.

By integrating the (kinetic) Vlasov-Maxwell equations numerically, we have found that the generation of small scales stops as soon as the scale length of the perturbation $2\pi/k$ and the electron gyroradius ϱ_e become of the same order and comparable to the electron skin depth. For the parameters of interest, i.e., for wavelengths of the order of d_e and stream velocities approaching the velocity of light, this result agrees with that obtained from a magnetic trapping mechanism in [18], in which case saturation occurs when the magnetic bounce frequency is comparable to the growth rate.

Kinetic saturation is produced by the spread in the phase space (v_x, v_y) of the electron velocities in the direction perpendicular to that of the initial beams. At saturation this spread is of the order of the initial velocity difference of the two beams. This is in agreement with the evolution of the gyroradius which, after a time transient that depends on the initial velocities of the electron beams, saturates at a value of order 1. The reference electron gyroradius ϱ_e measures the strength of the magnetic field B_z and the characteristic size of the electron orbits. The magnetic field B_z generated by the instability is strongly inhomogeneous and has different polarities in different regions. In the regions where B_z goes through zero the characteristic size of the electron orbits can be estimated as $(l\rho)^{1/2}$, where ρ is the electron gyroradius far from the inversion region and l is the scale length of the magnetic field inhomogeneity.

It is worth noticing that in the kinetic regime the Fourier spectrum of the magnetic field, as well as of all the other quantities, is characterized by a power law slope in the range $k_0 \leqslant k < 2\pi/d_e$, and by an exponential cutoff at larger wave numbers.

To study the magnetic field generation efficiency of the Weibel instability, we have performed a number of runs varying the beam velocities and symmetry. For two initially symmetric beams we have found that, when the beam velocities are much greater than the thermal speed, the conversion efficiency can be rather large for velocities of the order of $0.6c$, leading to approximate equipartition between kinetic and magnetic energy. On the other hand, when the beams are nonsymmetric the efficiency drops significantly.

The analysis presented in this paper refers to a spatially uniform initial configuration. In Ref. [11] it was shown that in an inhomogeneous plasma the linear evolution of the Weibel instability has a resonant-type behavior and that a spatial singularity is formed. This provides a mechanism for the formation of small scales additional to the nonlinear effects described in Sec. II C. We can expect that in an inhomogeneous plasma the formation of this resonant spatial singularity will be stopped at a spatial scale length of the order of the electron skin depth by kinetic effects analogous to those studied in this paper.

ACKNOWLEDGMENTS

We acknowledge the Cineca supercomputing center of Bologna and the Scuola Normale Superiore of Pisa for the use of their Cray T3D-T3E (INFM research project) and CM200, respectively. One of us, Francesco Califano, is glad to acknowledge Dr. Marco Voli (Cineca) for numerical suggestions on the use of the Cray T3D-T3E.

[1] M. D. Perry and G. Mourou, Science **264**, 917 (1994).
[2] M. Tabak, Y. Hammer, M. E. Glinsky, W. R. Kruer, S. C. Wilks, J. Woodworth, E. M. Campbell, M. D. Perry, and R. J. Mason, Phys. Plasmas **1**, 1626 (1994).
[3] T. Tajima and J. M. Dawson, Phys. Rev. Lett. **43**, 267 (1979).
[4] M. Everet, A. Lai, D. Gordon, C. E. Clayton, and C. Joshi, Nature (London) **368**, 527 (1994).
[5] R. Bingham, Nature (London) **368**, 496 (1994).
[6] M. G. Haines, Can. J. Phys. **64**, 912 (1986).
[7] E. Weibel, Phys. Rev. Lett. **2**, 83 (1959).
[8] V. Yu. Bychenkov *et al.*, Zh. Eksp. Teor. Fiz. **98**, 1269 (1990) [Sov. Phys. JETP **71**, 79 (1990)].
[9] G. A. Askar'yan, S. V. Bulanov, F. Pegoraro, and A. M. Pukhov, Pis'ma Zh. Eksp. Teor. Fiz. **60**, 251 (1994) [JETP Lett. **60**, 241 (1994)].
[10] G. A. Askar'yan, S. V. Bulanov, F. Pegoraro, and A. M. Pukhov, Comments Plasma Phys. Control Fusion **17**, 35 (1995).
[11] F. Califano, F. Pegoraro, and S. V. Bulanov, Phys. Rev. E **56**, 963 (1997).
[12] F. Pegoraro, S. V. Bulanov, F. Califano, M. Lontano, Phys. Scr. **T63**, 262 (1996).
[13] N. A. Krall and A. W. Trivelpiece, in *Principles of Plasma Physics* (San Francisco Press, San Francisco, 1986), p. 491.
[14] S. V. Bulanov and P. V. Sasorov, Fiz. Plazmy **4**, 746 (1978) [Sov. J. Plasma Phys. **4**, 746 (1978)].
[15] S. V. Bulanov, F. Pegoraro, and J. Sakai, *Variety of Nonlinear Wave-Breaking*, 13th Advanced International Committee for Future Accelerators, Beam Dynamics Workshop and 1st ICFA Novel and Advanced Accelerator Workshop: the Second Generation Plasma Accelerators, July 1997, Kyoto, Japan [Nucl. Instrum. Methods Phys. Res. (to be published)].
[16] G. Kalman, C. Montes, and D. Quemada, Phys. Fluids **11**, 1797 (1968).
[17] N. W. Albright, Phys. Fluids **13**, 1021 (1970).
[18] R. C. Davidson, D. A. Hammer, I. Haber, and C. E. Wagner, Phys. Fluids **15**, 317 (1972).